

Design of a Microwave Time Reversal Mirror for Imaging Applications

Saptarshi Mukherjee*, Lalita Udpa, Yiming Deng,
Premjeet Chahal, and Edward J. Rothwell

Abstract—This paper presents a design of microstrip transmitting and receiving antennas to be used for time reversal ultra-wideband imaging applications. The transmitter and receiver arrays are together known as a time reversal mirror (TRM). Based on the properties of time reversal and its imaging applications, an antipodal Vivaldi antenna and a monopole antenna are proposed for the transmitter and receiver designs, respectively. Simulation and measurement results demonstrate the efficiency of the antennas for a time reversal mirror. The overall system is demonstrated for source and target imaging applications.

1. INTRODUCTION

Time reversal (TR) is based on the reciprocity property of the wave equation. The time reversed electric and magnetic field components back-propagate to focus at the source location. TR was introduced by Mathias Fink in 1992 for ultrasonic imaging and later widely utilized in several ultrasonic applications such as transcranial therapy [1]. It was extended into the realm of electromagnetics by Lerosey et al. [2] and has shown a lot of progress in ultra-wideband (UWB) applications involving radar detection in cluttered media [3] and non-destructive evaluation [4]. Research on using microwave TR for imaging has been limited over the years, but warrants renewed study because of its advantages over conventional imaging systems. These advantages include its non-iterative nature and its super-resolution and selective focusing capabilities [5].

Numerous microstrip antennas have been proposed to cover the UWB frequency band between 3.1 and 10.6 GHz released by the Federal Communications Commission for short-range wireless applications. Designing UWB antennas for imaging applications is challenging since unlike narrow-band antennas, UWB antennas must exhibit near-uniform radiation characteristics such as high gain, return losses and low cross-polarization, over large bandwidths. Moreover, the design of UWB time reversal antennas (TRAs) is particularly challenging, since the antennas need to comply with the unique properties of time reversal. The TRA needs to illuminate most of the region of interest effectively and detect potential anomalies in presence of other significant scatterers. A lot of different UWB antennas proposed recently do not satisfy these requirements. For example, the UWB antenna presented in [7], though having small size, lacks both reasonable gain and return losses. Additionally, previous research on microstrip TRA designs has proposed using the same transmitting and receiving antenna [8], which is not desirable for time reversal.

This research proposes a novel design of a time reversal mirror (TRM) for imaging applications. Separate UWB transmitting and receiving antennas operating between 3 to 10 GHz are designed, keeping in consideration the unique features of TR imaging. Comparison between simulation and measurement

Received 18 May 2017, Accepted 21 August 2017, Scheduled 3 September 2017

* Corresponding author: Saptarshi Mukherjee (mukher40@egr.msu.edu).

The authors are with the Department of Electrical and Computer Engineering, Michigan State University, East Lansing, MI 48824, USA.

results shows good correlation. The proposed TRM has been validated by performing an imaging experiment using a pulsed time domain laboratory setup, coupled with a back-propagation 2D FDTD code. Experimental results validate the system's efficiency and lay the foundation for potential imaging applications.

2. DESIGN OF AN ANTENNA SYSTEM FOR TIME REVERSAL

The design of the TRA is non-trivial due to several reasons. The contributing factors are as follows

- (i) Bandwidth. TR is similar to phase conjugation in optics. The range resolution is governed by the pulse width, with smaller pulse width leading to better detection. A short time-domain pulse has a half-amplitude bandwidth given by the following relation [9]:

$$\Omega = \frac{1}{\pi\tau} 4 \ln(2), \quad (1)$$

where Ω and τ are the bandwidth and pulse width, respectively. Thus, both the transmitting and receiving antennas should be designed to operate over a wide bandwidth.

- (ii) Radiation Pattern. The transmitting antenna needs to have a beam narrow enough to illuminate the region of interest efficiently with a large gain. However, the beam cannot be too focused, since TR theory is based on waves diverging outwards from a point source. In contrast, TR theory assumes the receiver array to be point receivers [10]. Thus the receiving antennas should behave in radiation mode as point sources having omnidirectional radiation patterns. Since the radiation pattern for the transmitting antenna needs to be different from that of the receiving antenna, the same antenna cannot be used as both transmitter and receiver.
- (iii) Polarization. The confinement of the electric or magnetic field along the plane of propagation leads to linear polarization. However, antennas may have field components orthogonal to the direction of propagation, leading to cross-polarization. Cross-polarized electric field components from the transmitting antenna are lost when using a 2D image reconstruction algorithm, thus degrading the overall imaging quality of the 2-D algorithm [11]. In order to reduce the undesired field components, the cross polarization of the antenna should be maintained as low as possible.

Simulation studies for antenna design were performed using the commercial high frequency electromagnetic field simulation software Ansys HFSS. The antennas were fabricated using conventional photolithography. Reflection coefficients were measured using an Agilent N5227A network analyser, and radiation patterns were measured using a SATIMO Starlab near-field measurement system.

3. TRANSMITTING ANTENNA

Based on the crucial factors of the TRA discussed above, a modified slot-edged antipodal Vivaldi (SE APV) antenna is chosen as the transmitting antenna. Introduced by Gibson in 1979 [12], the Vivaldi antenna serves as a potential candidate for wide-band applications due to its broad impedance bandwidth and ease of planar structure integration. In conventional Vivaldi antennas, the transition from microstrip to slotline restricts extension of impedance bandwidth and generates high cross-polarization due to asymmetric feeding. With the Vivaldi antenna, the bandwidth limitation due to the microstrip to slot-line transition can be removed by choosing a proper feed. One solution used in this manuscript is to use a microstrip to stripline or a two-sided slotline transition [13], as recently used by many researchers [14, 15]. Thus, no external balun is required to operate with unbalanced transmission lines that are typically used as microwave feed networks [16].

3.1. Design Parameters

An exploded top-view design of the proposed antenna, along with its dimensions is shown in Fig. 1(a). The fabricated antenna is shown in Fig. 1(b). In this design, the tapered slots are modeled as elliptical transitions, with the curve defined as

$$y = b\sqrt{1 - \frac{x^2}{a^2}}, \quad (2)$$

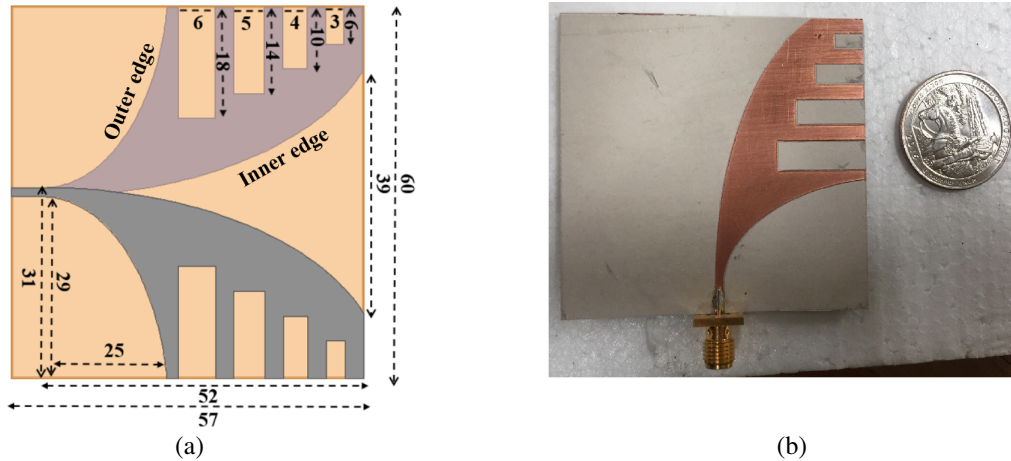


Figure 1. Design of the proposed transmitting antenna. (a) Vivaldi design (mm). (b) Fabricated antenna (US quarter dollar shown for comparison).

By choosing a substrate (Rogers RT Duroid 6010) with a high dielectric constant of $\epsilon_r = 10.2$, the antenna size is miniaturized to $6\text{ cm} \times 5.7\text{ cm}$. Although an increased antenna size reduces the lower end frequency of operation, the antenna needs to be small enough to be integrated into imaging applications such as breast tumor detection.

The key parameters that determine the performance of the antenna include: a) elliptical axes of the inner and outer edges, b) microstrip line dimensions, and c) slot dimensions. The inner edge is primarily responsible for the current flow, since most of the current is confined along the inner edge during the operation of the antenna. Since the opening rate of the edge decides the current concentration, it is a critical parameter for antenna design. The key factor in determining the lower end frequency is the opening width. Since the Vivaldi antenna operates as a resonant antenna at the lower frequency end (f_m), the initial antenna opening width (W_{in}) can be estimated by the following expression [12, 17]:

$$W_{in} = \frac{c}{2f_m\sqrt{\epsilon_e}}, \tag{3}$$

where f_m is the minimum frequency, and ϵ_e is the effective dielectric constant of the antenna. The relationship between radiation properties and the outer edge has been extensively studied in [18]. Although the dominant current flows along the inner edge, a sharp increase in the outer edge sets up current along the outer edge. This effect produces a narrower mainbeam and higher sidelobes. The major axis of the inner and outer edges and the microstrip line dimensions were optimized using HFSS with respect to its UWB performance, with the constraint of keeping the antenna size as small as possible. From Eq. (3) and optimization based on HFSS simulations, W_{in} is finally calculated to be around 39 mm.

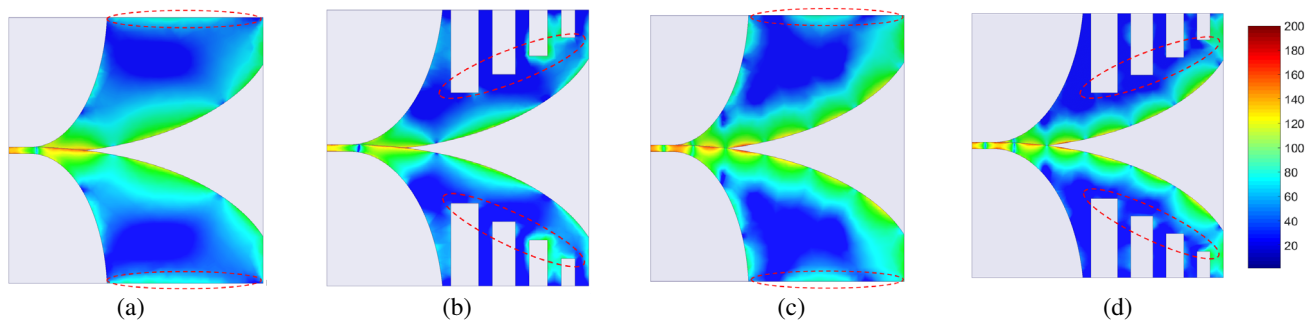


Figure 2. Current density for APV vivaldi (Units in A/m): (a) 4 GHz, (c) 8 GHz, SE APV antenna : (b) 4 GHz, (d) 8 GHz. (a) APV: 4 GHz. (b) SE APV: 4 GHz. (c) APV: 8 GHz. (d) SE APV: 8 GHz.

3.1.1. SE APV Antenna

The surface current distribution for a conventional APV antenna shows strong edge currents, marked in the dashed-line region A of Figs. 2(a), (c). The currents radiate vertically, leading to undesired side and back lobes. In order to reduce these surface currents, four slots are etched at the ends of the twin lines of the antenna to form the SE APV antenna. As seen from Figs. 2(b), (d), the modification is capable of eliminating the unwanted currents at the edges. This leads to an enhanced end fire direction radiation and thus weakens the back-direction radiation.

3.2. Antenna Characteristics in the UWB range

The comparison of simulated and measured reflection coefficients, given in Fig. 3(a), shows good correlation. The slight difference in the measured and simulation results possibly arises due to soldering inaccuracies, introduction of the $50\ \Omega$ SMA connector for feeding the antenna or fabrication errors. It is noted that $|S_{11}| \leq 10$ dB over the entire band. Additionally, the impact of a small metallic cylindrical target (radius and height 5 mm) in the near-field (1 cm away) of the antenna is observed from Fig. 3(a). The $|S_{11}|$ results show sensitivity due to the presence of the target throughout the frequency band of 3 to 10 GHz.

The radiation properties of an antenna vary, depending on the near-field and far-field ranges of the antenna. The far-field region is commonly expressed to exist at distances greater than $2D^2/\lambda$ [17], where D is the maximum dimension of the antenna, and λ is the wavelength. For a UWB antenna, the far-field distance varies depending on the frequency. For the proposed antenna, the far-field ranges vary approximately between 0.1 m and 0.5 m. For efficient imaging applications, the sample to be imaged needs to be in close proximity of the antenna. The antenna may operate in far-field or near-field ranges depending on the distance between the antenna and the imaging region. Hence the radiation properties of the antenna need to be studied for both ranges.

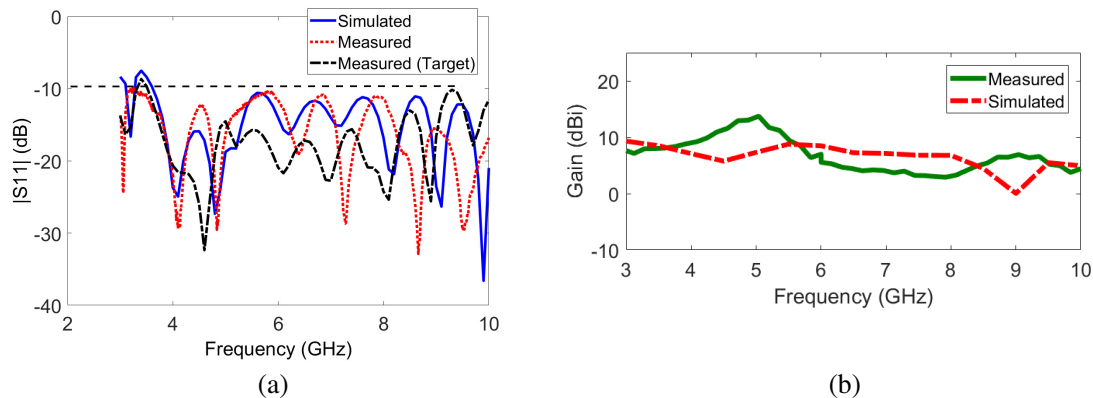


Figure 3. Transmitting antenna performance. (a) Reflection coefficients comparison. (b) Maximum realized gain comparison.

3.2.1. Far Field Radiation Patterns

Some of the crucial elements such as gain, radiation pattern and polarization of the antenna can be determined from the far-field radiation characteristics of the antenna. As shown in Fig. 3(b), the comparison between the simulated and measured boresight gains of the antenna shows slight discrepancies; however, the measured realized gain is greater than 5 dBi in most of the frequency band. A maximum measured gain of 14 dBi is achieved at 5 GHz. The simulated and measured radiation patterns at 4, 6 and 8 GHz (Figs. 4(a), (b), (c)) show good correlation. The antenna shows nice end-fire performance with the main lobe aligned along the direction of the tapered slots. All the operating frequencies maintain the same polarization plane and similar radiation patterns. The transmitting

antenna has an uniformly narrow beam with a moderately large gain throughout the frequency range. However, the beam is not too focused, which is ideal from the time reversal point of view. As discussed before, the cross polarization of the transmitting antenna should be maintained as low as possible. It is noticed that the cross-polarized gain is much lower than the co-polarized gain throughout the frequency range, with a minimum difference at boresight of 8 dB. The presence of strong horizontal components of the surface current radiating electric fields along the sides lead to relatively high cross-polarization in the E plane.

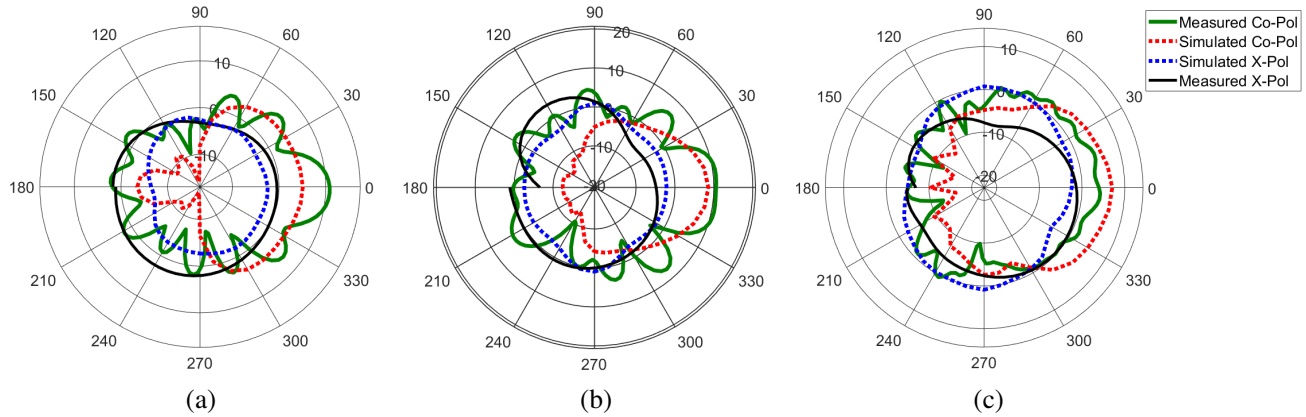


Figure 4. Transmitting antenna far field realized gain radiation pattern. (a) E Plane: 4 GHz. (b) E Plane: 6 GHz. (c) E Plane: 8 GHz

3.2.2. Near Field Radiation Patterns

The near-field radiation pattern for the transmitting antenna was computed using HFSS at 2 cm radial distance from the apex of the antenna. Figs. 5(a) and 5(b) present the magnitude of the simulated radiated electric fields in the E -plane at 4 GHz, 6 GHz and 8 GHz. As seen from Fig. 5(a), the E -plane radiation pattern is uniform with the intensities almost equal at all frequencies. The beam is relatively uniform with a half-power beamwidth (HPBW) of 41.2°, 32.7° and 30° at 4 GHz, 6 GHz, and 8 GHz, respectively. However, the presence of relatively high intensity side lobes (−4.8 dB for 4 GHz) might degrade the imaging quality. Hence, special attention needs to be taken so that the size of the sample to be imaged is less than or equal to the HPBW of the antenna. Similar radiation intensities noted at all frequencies at $\theta = 90^\circ$, $\phi = 90^\circ$ ensure that the peak realized gain is uniform at all frequencies in the near-field range. The simulated E-field distributions, depicted in Figs. 5(b), (c) for 6 GHz and 10 GHz on xy -plane, show the fields spreading along the tapered slot region and radiating from the top edge of the antenna, thus displaying strong end-fire radiation characteristics.

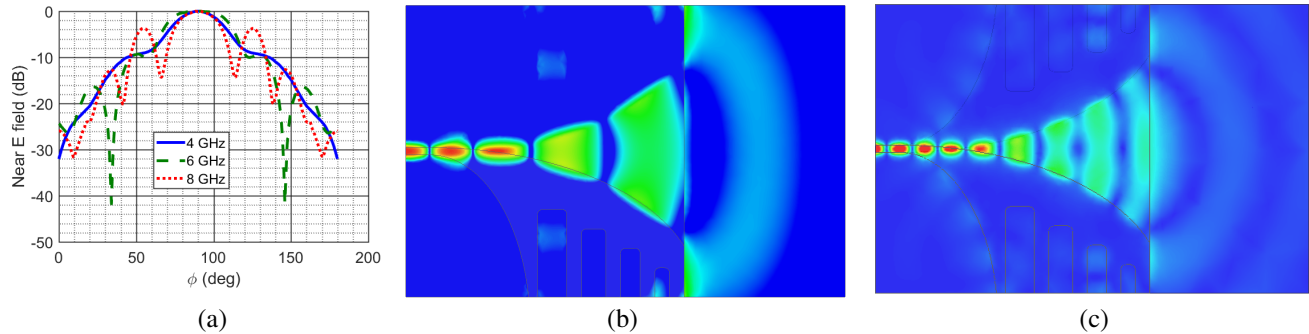


Figure 5. Transmitting antenna near E -field pattern. (a) E plane near field radiation pattern. (b) Electric field: 6 GHz. (c) Electric field: 10 GHz.

4. RECEIVING ANTENNA

As mentioned before, TR theory assumes the receiver array to be point receivers, along with UWB performance. Thus, ideally the receiving antennas should have omnidirectional radiation patterns. Conventional monopole antennas have several advantages such as low cost, ease of fabrication and omnidirectional radiation pattern in the transverse plane, but do not yield large bandwidths [17]. Recently, several approaches and techniques have been proposed to tailor the antenna towards wideband applications. In the regime of wideband antennas, planar monopole antennas [7] have garnered huge recognition due to their flat structure, small size and ease of integration. A planar monopole replaces the conventional wire-element based monopole design with a planar element. In this research, a reduced-ground slotted rectangular (RGSR) monopole is selected as the receiving antenna. The theoretical resonance frequency (f_t) for the fundamental mode of the antenna can be calculated according to Eq. (3).

The design starts off with an initial monopole antenna with a reduced ground plane and without any feed step. The reduced ground plane is responsible for the wide bandwidth of the antenna, due to absence of fringing fields between the radiating patch and the ground plane. The length of the ground plane is reduced to $\frac{\lambda}{10}$ at the lower frequency end. However, this antenna is matched only at the lower and higher frequency limits. A double-feed step between the microstrip line and the radiating patch behaves as quarter wave transformers, thus improving the impedance bandwidth. The blending ground plane edges help in matching at the higher frequencies. The two L-shaped slots (smoothed) in the ground plane further help in impedance matching and thus enhance the bandwidth of the antenna and help miniaturize it to an area of 3.5 cm by 3.2 cm. Fig. 6 shows the effects of step by step evolution of

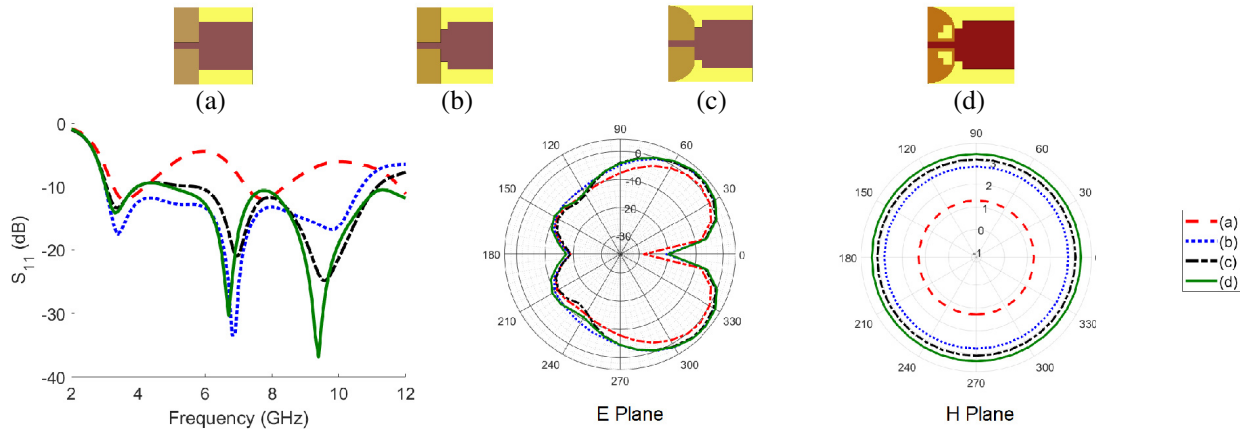


Figure 6. Monopole antenna design and its evolution.

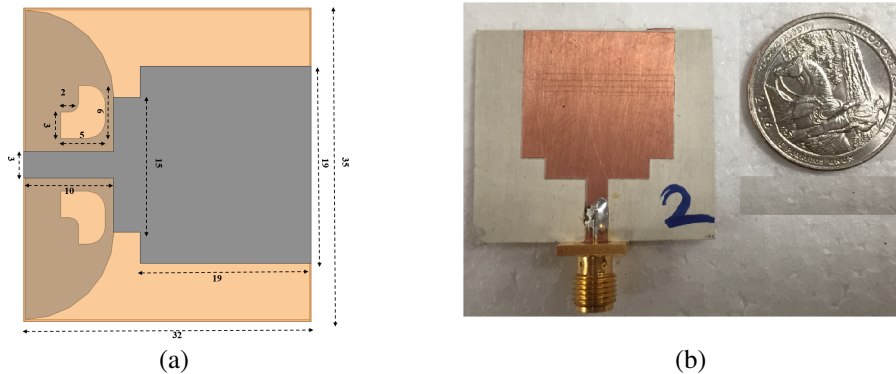


Figure 7. Receiving antenna. (a) Monopole design (mm). (b) Fabricated monopole antenna.

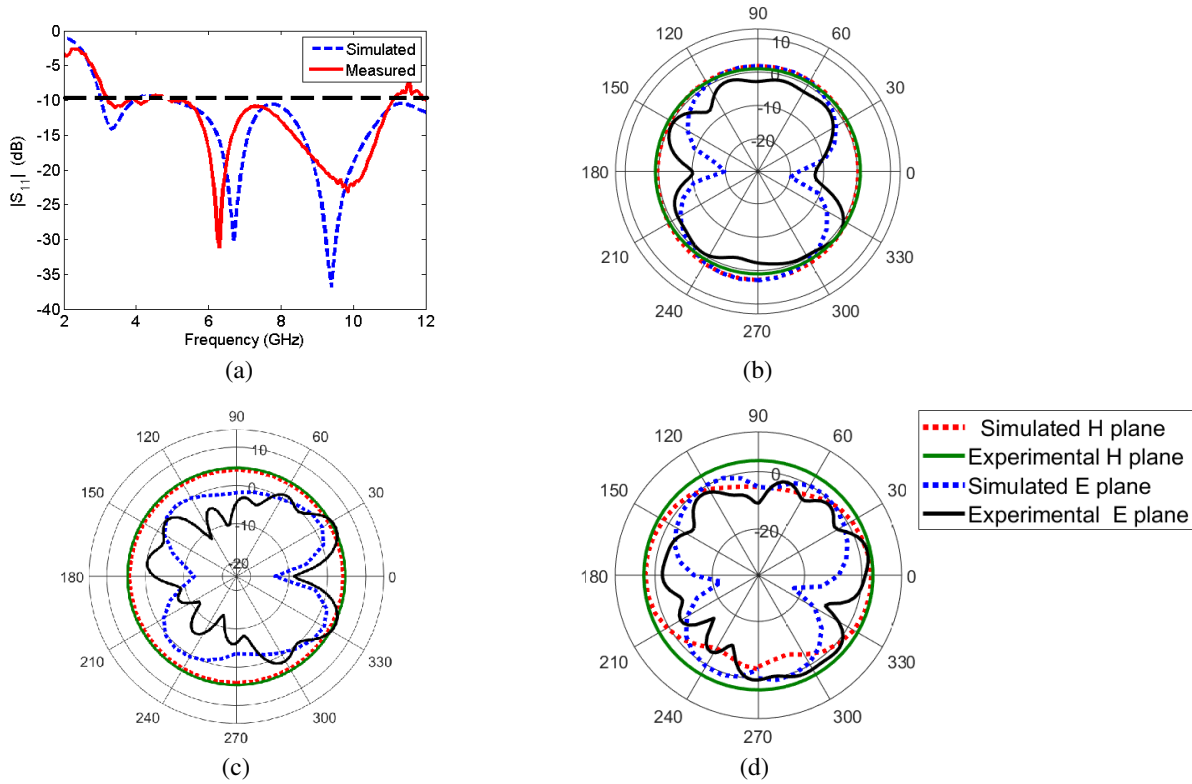


Figure 8. Proposed receiving antenna and its performance. (a) Reflection coefficients comparison. (b) Radiation pattern: 4 GHz. (c) Radiation pattern: 6 GHz. (d) Radiation pattern: 10 GHz.

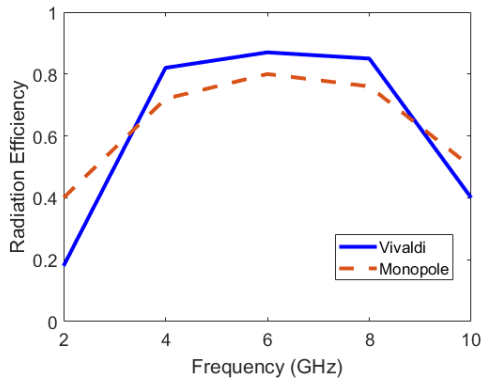


Figure 9. Radiation efficiency of the antennas.

Antenna	BW	ρ (cm)	G (dB)
SE APV	3.5	6	14
[14]	5.6	6	10
[15]	3	8	11.5
RGSR	3.5	3.5	4.2
[7]	2.1	3.5	3.6
[19]	3.5	4.1	4

Table 1. Comparison of different antennas.

the antenna, as mentioned above. A monopole-like radiation pattern with nulls appearing at the center for the E plane omnidirectional radiation in the H plane is observed, with the final evolved design (d), providing the maximum gain.

An exploded top-view design of the RGSR monopole antenna and its dimensions are shown in Fig. 7(a). FR4, with a dielectric constant of $\epsilon_r = 4.4$, is selected as the substrate since it is inexpensive, thus reducing the cost of fabrication. The fabricated antenna is shown in Fig. 7(b). The comparison of the simulated and measured reflection coefficients given in Fig. 8(a) show that $|S_{11}| < -10$ dB over the entire bandwidth. The simulated and measured E -plane radiation patterns exhibit a monopole-like radiation as shown in Fig. 8(b). A maximum gain of 4.2 dB is achieved at 6 GHz.

An examination of the radiation efficiency of the two antennas shows near constant values across the

specified band of approximately 80–85%, as seen in Fig. 9. A comparison of the performance (fractional bandwidth (BW), maximum size (ρ) and maximum gain (G)) of the designed antennas with Vivaldi and planar monopole antennas described in the literature is presented in Table 1. It is observed that the achieved gain of the SE-APV antenna is much more than that of the antennas presented in [14, 15], while maintaining a small size and comparable BW. Similarly, the RGSR antenna achieves higher gain and BW than the UWB antennas proposed in [7, 19], while maintaining a comparable size. Besides the improved antenna performance, the concept of using different transmitter and receiver antennas, as well as choosing specific antenna types in order to implement TR for imaging applications, is introduced in this research. Using different antennas is greatly desirable due to several factors as mentioned in Section 2.

5. TIME DOMAIN CHARACTERIZATION

The antenna system is to be integrated into a time-domain setup and used in a TR algorithm. The quality of the received pulse is directly related to the quality of the temporal focusing of TR. Hence, the antenna system needs to be characterized in the time domain. An HFSS simulation is performed with the transmitting and receiving antennas separated by a distance 150 mm, as shown in Fig. 10(a).

5.1. Group Delay

A critical parameter for a UWB antenna is the group delay, which measures the time signal distortion introduced by the antenna. In an ideal, distortionless signal transmission, the antenna system has a constant group delay (linear phase response) over the whole bandwidth. Equal group delay for all frequencies in a signal ensures that the signal received by the antenna system has the same shape as the transmitted signal. Fig. 10(b) illustrates the group delay vs frequency for the configuration. Although the group delay is not constant throughout the frequency range, the plot shows an average group delay value of approximately 1.2 ns, with a few deviations between 8.5 and 9 GHz. Thus the antenna system can be reliably used for transmitting a short pulsed signal and receiving the scattered signal without serious distortion.

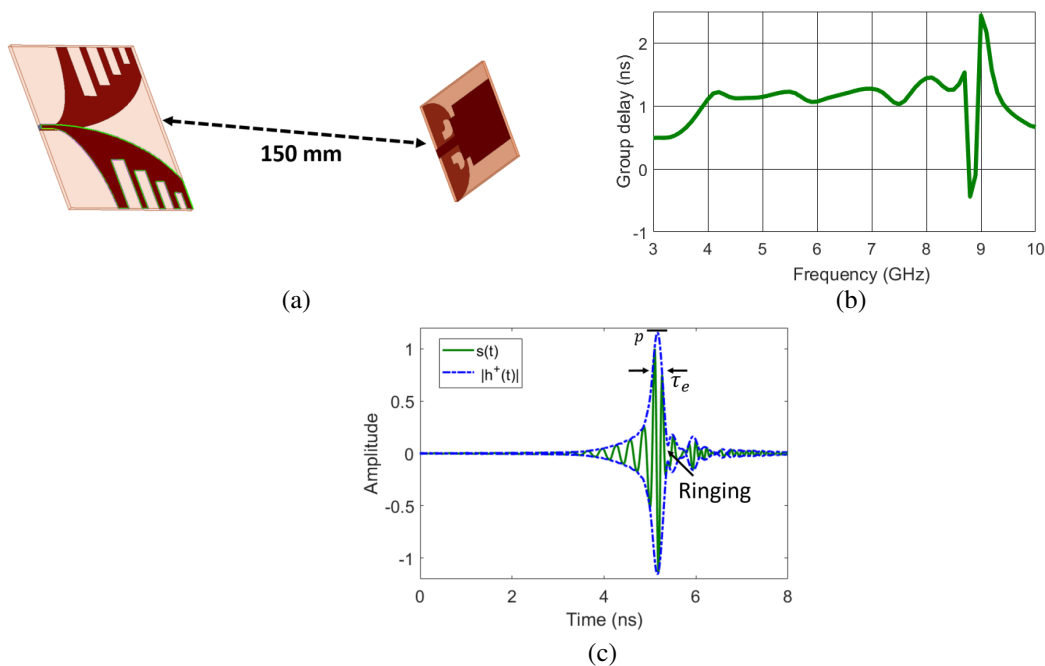


Figure 10. Time-domain analysis for the TRA. (a) TRA configuration. (b) Group delay of the TRA. (c) TRA time-domain transient response

5.2. Time Domain Response

The transient response for the specific configuration shown in Fig. 10(a) is also studied. The received signal $s(t)$ can be represented by a convolution of the impulse response, as given by the following expression [6]:

$$s(t) = u_{Tx}(t) * h_{Tx}(t, \theta, \phi) * h_{ch}(t) * h_{Rx}(t, \theta, \phi). \quad (4)$$

Here u_{Tx} is the transmitted signal, and h_{Tx} , h_{ch} and h_{Rx} are the transmitting antenna, medium channel and receiving antenna impulse response functions, respectively. For the schematic shown in Fig. 10(a), the complex S_{21} measurements are transformed into the time domain to obtain the received time pulse. The received time signal is shown in Fig. 10(c). The antenna dispersion can be analyzed from its analytic impulse response, which is calculated by the Hilbert transform \mathcal{H} of $s(t)$, given by $h^+(t)$ [6]. The envelope $|h^+(t)|$ localizes the energy distribution versus time and thus measures the dispersion of an antenna. The specific quantities investigated in this case are:

- Peak Value of envelope $p(\theta, \phi)$. This quantity is a measure of the maximum value of the strongest peak of the time domain response. A high peak value is desirable, since it ensures a stronger peak. As seen from Fig. 10(c), a value of $p(\theta, \phi)$ of 1.16 is achieved.
- Envelope width τ_e . The envelope width is a measure of the temporal broadening of the radiated impulse. Practically, τ_e should be small in order to obtain high resolution and data rate. The range resolution is governed by τ_e , with smaller pulse width leading to better resolution. The envelope width can be obtained from the full width at half maxima of the envelope. As seen from Fig. 10(c), a τ_e value of 160 ps is achieved.
- Ringing. Several factors such as multiple reflections in the antenna are responsible for oscillations of the received pulse after the main peak, as observed from Fig. 10(c). This phenomenon is known as ringing. Ideally, the duration of ringing (τ_r) should be less than a few τ_e . Specifically, a high value of τ_r is undesirable for temporal focusing of the time reversed electromagnetic fields. The time duration within which the envelope has fallen from $p(\theta, \phi)$ to a lower bound $\alpha \cdot p(\theta, \phi)$ is measured as τ_r . As seen from Fig. 10(c), a value of τ_r for $\alpha = 0.1$ of 200 ps is achieved.

6. EXPERIMENTAL RESULTS

A passive TR experiment for imaging a metallic cylinder (radius 1.6 cm) was conducted using a pulsed time domain laboratory setup and a FDTD 2D code for back-propagation of the TR fields [20]. The experimental configuration and setup are shown in Figs. 11(a) and 11(b) and explained in details in [20]. A small arch range of radius 10 cm with a circular platform was used to position the antennas. The receiving monopole antenna was moved, while keeping the transmitting Vivaldi antenna stationary, in order to emulate the receiver array system. The time domain system generates a pseudo-Gaussian pulse signal of bandwidth 10 GHz, which is fed as input to the Vivaldi antenna.

The setup is a miniaturized version of [20], tailored for precise near field imaging applications, such as micro-cracking detection in composite NDE and breast tumor diagnosis in medical imaging. While the experiments in [20] are meant for far-field detection purposes only, the present setup can work both in transmission and reflection modes (with 350 degrees coverage) as a near-field and far-field system, in order to gain better imaging quality. Since all parts of the setup, including the sample stand and antenna stands, can be adjusted, it is possible to measure cross-polarized field components and thus the potential for performing 3D imaging. Moreover, while horn antennas were used in [20] for target localization experiments in the reflectivity arch-range, they could not be utilized for near-field imaging in the mini-arch range setup, since they produce a plane wave at far-field distances (~ 3.5 m) and are intended for diffraction limited imaging. Additionally, the relatively large size and 3D structure of the horn antennas make them undesirable for compact imaging applications due to inefficient illumination of the imaging domain, size and weight constraints and their inability to be integrated into planar circuits. Hence the designed planar microstrip antennas are preferred candidates for the mini arch-range setup shown in Fig. 11(a).

The scattered fields from the target are recorded by the monopole antenna. These fields are time reversed and back-propagated using the numerical model. At the localized time instant, the electric

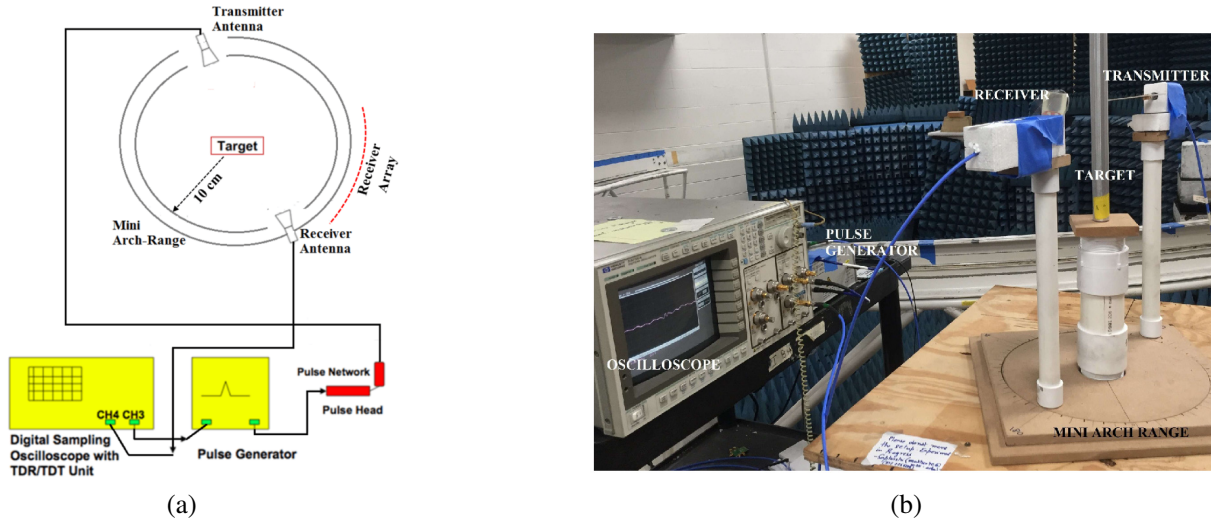


Figure 11. (a) Time domain scattering measurement configuration. (b) Experimental setup.

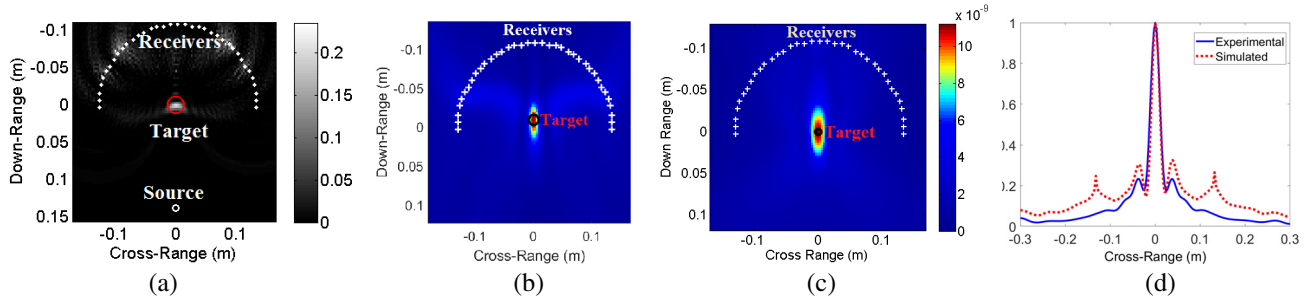


Figure 12. Target imaging experiment: (a) Electric fields focused at metal rod. (b) Simulated energy image. (b) Experimental energy image. (d) Cross-range signal comparison.

fields are efficiently focused at the metal target location, as displayed in Fig. 12(a). The time integrated electric energy shows the energy localized around the target region, as displayed in Fig. 12(c). The full width at half maximum (1.8 cm) of the cross range energy signal, indicated by the solid black line of Fig. 12(d) can be utilized to estimate the actual size of the target. A simulation is performed for the similar configuration using 2D FDTD codes, demonstrating excellent comparison between experimental and simulated results, as shown in Figs. 12(b), (c) and (d)).

7. CONCLUSION

Microstrip transmitting and receiving antennas, operating between 3 GHz and 10 GHz, are designed to be used in a TRM for imaging applications. A TSE APV antenna and an RGSR monopole antenna are proposed and developed as the transmitting and receiving antennas of the system. The efficacy of the transmitting antenna was evaluated at both far- and near-field ranges. The antennas are optimized according to the requirements of the system, characterized in both frequency and time domain, and fabricated. There is good match between simulation and measurement results. Measurement results show that both antennas meet the requirements for a TR system. Accurate measurement results demonstrate the feasibility of the TRA for imaging applications. The imaging system can be used in several applications such as complicated long range radar imaging, rapid inspection of composites and breast tissue imaging. Future work involves evaluating the super-resolution capabilities of TR and testing the robustness of the system for detection of tumors in realistic multi-layered breast phantoms as well as nondestructive evaluation of composite structures.

REFERENCES

1. Thomas, J.-L. and M. A. Fink, "Ultrasonic beam focusing through tissue inhomogeneities with a time reversal mirror: application to transskull therapy," *IEEE Trans. Ultrason., Ferroelect., Freq. Control*, Vol. 43, No. 6, 1122–1129, Nov. 1996.
2. Lerosey, G., J. De Rosny, A. Tourin, A. Derode, G. Montaldo, and M. Fink, "Time reversal of electromagnetic waves," *Phys. Rev. Lett.*, Vol. 92, No. 19, 193904, 2004.
3. Zhang, W., A. Hoorfar, and L. Li, "Through-the-wall target localization with time reversal music method," *Progress In Electromagnetics Research*, Vol. 106, 75–89, 2010.
4. Rodríguez, S., N. Lei, B. Crowgey, L. Udpa, and S. S. Udpa, "Time reversal and microwave techniques for solving inverse problem in non-destructive evaluation," *NDT & E Intl.*, Vol. 62, 106–114, 2014.
5. Devaney, A. J., E. A. Marengo, and F. K. Gruber, "Time-reversal-based imaging and inverse scattering of multiply scattering point targets," *J. Acoust. Soc. Am.*, Vol. 118, No. 5, 3129–3138, 2005.
6. Wiesbeck, W., G. Adamiuk, and C. Sturm, "Basic properties and design principles of UWB antennas," *Proceedings of the IEEE*, Vol. 97, No. 2, 372–385, 2009.
7. Lim, K.-S., M. Nagalingam, and C.-P. Tan, "Design and construction of microstrip UWB antenna with time domain analysis," *Progress In Electromagnetics Research M*, Vol. 3, 153–164, 2008.
8. Nadia Maaref, P. M., X. Ferrières, C. Pichot, and O. Picon, "Electromagnetic imaging method based on time reversal processing applied to through-the-wall target localization," *Progress In Electromagnetics Research M*, Vol. 1, 59–67, 2008.
9. Crowgey, B. R., E. J. Rothwell, L. C. Kempel, and E. L. Mokole, "Comparison of UWB short-pulse and stepped-frequency radar systems for imaging through barriers," *Progress In Electromagnetics Research*, Vol. 110, 403–419, 2010.
10. Fink, M., "Time reversal of ultrasonic fields. i. basic principles," *IEEE Trans. Ultrason., Ferroelect., Freq. Control*, Vol. 39, No. 5, 555–566, 1992.
11. Kosmas, P. and C. M. Rappaport, "FDTD-based time reversal for microwave breast cancer detection-localization in three dimensions," *IEEE Transactions on Microwave Theory and Techniques*, Vol. 54, No. 4, 1921–1927, 2006.
12. Gibson, P. J., "The Vivaldi aerial," *9th European Microwave Conference*, 101–105, IEEE, 1979.
13. Gazit, E., "Improved design of the Vivaldi antenna," *IEE Proceedings H (Microwaves, Antennas and Propagation)*, Vol. 135, 89–92, IET, 1988.
14. Kota, K. and L. Shafai, "Gain and radiation pattern enhancement of balanced antipodal Vivaldi antenna," *Electronics Letters*, Vol. 47, No. 5, 303–304, 2011.
15. Wang, P., H. Zhang, G. Wen, and Y. Sun, "Design of modified 6–18 GHz balanced antipodal Vivaldi antenna," *Progress In Electromagnetics Research C*, Vol. 25, 271–285, 2012.
16. Balanis, C. A., *Modern Antenna Handbook*, John Wiley & Sons, 2011.
17. Balanis, C. A., *Antenna Theory: Analysis and Design*, John Wiley & Sons, 2016.
18. Greenberg, M. C., K. L. Virga, and C. L. Hammond, "Performance characteristics of the dual exponentially tapered slot antenna (detsa) for wireless communications applications," *IEEE Transactions on Vehicular Technology*, Vol. 52, No. 2, 305–312, 2003.
19. Abbosh, A. M. and M. E. Bialkowski, "Design of ultrawideband planar monopole antennas of circular and elliptical shape," *IEEE Transactions on Antennas and Propagation*, Vol. 56, No. 1, 17–23, 2008.
20. Mukherjee, S., L. Udpa, S. Udpa, and E. Rothwell, "Target localization using microwave time reversal mirror in reflection mode," *IEEE Transactions on Antennas and Propagation*, Vol. 65, No. 2, 820–828, 2016.